RSC Advances

PAPER

View Article Online
View Journal | View Issue

Cite this: *RSC Adv.*, 2022, **12**, 1694

Solution combustion synthesis of Ni-based hybrid metal oxides for oxygen evolution reaction in alkaline medium†

Aymen S. Abu Hatab, [ab] Yahia H. Ahmad, [c] Mohd B. Abdul Rahman *[ab] and Siham Y. Al-Qaradawi *[c]

Oxygen evolution reaction (OER) has arisen as an outstanding technology for energy generation, conversion, and storage. Herein, we investigated the synthesis of nickel-based hybrid metal oxides ($Ni_xM_{1-x}O_y$) and their catalytic performance towards OER. $Ni_xM_{1-x}O_y$ catalysts were synthesized by solution combustion synthesis (SCS) using the metal nitrates as oxidizer and glycine as fuel. Scanning electron microscope (SEM) micrographs display a porous morphology for the hybrid binary $Ni_xM_{1-x}O_y$, the common feature of combusted materials. X-ray diffraction (XRD) of $Ni_xM_{1-x}O_y$ depicted well-defined diffraction peaks, which confirms the crystalline nature of synthesized catalysts. The particle size of as-synthesized materials ranges between 20 and 30 nm with a mesoporous nature as revealed by N_2-physisorption. The electrocatalytic performance of the as-prepared materials was evaluated towards OER in alkaline medium. Among them, $Ni_xCo_{1-x}O_y$ showed the best catalytic performance. For instance, it exhibited the lowest overpotential at a current density of 10 mA cm^{-2} (404 mV), onset potential (1.605 V), and Tafel slope (52.7 mV dec^{-1}). The enhanced electrocatalytic performance of $Ni_xCo_{1-x}O_y$ was attributed to the synergism between cobalt and nickel and the alteration of the electronic structure of nickel. Also, $Ni_xCo_{1-x}O_y$ afforded the highest Ni^{3+}/Ni^{2+} when compared to other electrocatalysts. This leads to higher oxidation states of Ni species, which promote and improve the electrocatalytic activity.

Received 30th September 2021
Accepted 22nd December 2021

DOI: 10.1039/d1ra07304d

rsc.li/rsc-advances

Introduction

The dramatic increase in the global energy demand, together with a growing environmental hazard resulting from fossil fuels, has triggered researchers' attention for developing new benign and clean sources of energy.[1–3] The oxygen evolution reaction (OER) has grown to prominence as a critical technique in energy generation, conversion, and storage, such as hydrogen production *via* water electrolysis,[4–6] regenerative fuel cells,[7,8] and rechargeable metal-air batteries.[9–11] Noble metals and their composites show enhanced catalytic performance towards OER, such as Pt, RuO_2, and IrO_2.[12–14] However, the large-scale employment of these catalysts is hindered due to their low abundance, high cost, and/or low stability.[15,16] For instance, in alkaline medium, Pt shows low activity caused by the formation of insulating platinum oxides, while RuO_2 suffers from low stability at high potentials due to the generation of higher-valent ruthenium oxides.[17]

In the last few decades, several researchers have synthesized and developed alternative electrocatalysts such as transition metal oxides and perovskites. These electrocatalysts are based on low-cost, stable, and earth-abundant nature metals such as Ni, Co, Fe, Mn, and Mo.[18–21] Among them, nickel-based catalysts received considerable interest attributed to their high stability in alkaline media, low cost, and enhanced OER activity.[4,7] For instance, Babar and co-workers synthesized a porous nano-wall NiO loaded directly on bare nickel foam; it exhibits remarkable OER electrocatalytic performance with an overpotential of 310 mV at a current density of 10 mA cm^{-2} and a Tafel slope of 54 mV dec^{-1}, as well as enhanced OER durability and long-term stability (up to 24 hours).[22]

One of the reported approaches to enhance the reactivity of NiO is the mixing with other metal oxides, which is called the mixed transition metal oxides (MTMO) approach. MTMO have arisen as potential candidates for OER due to their high stability and outstanding electrochemical properties.[23,24] In this regard, Ni has been coupled with several earth-abundant metals such as Co, Fe, Mn, Mo, and Cu.[21,25–28] The hybrid materials show higher electrocatalytic activity and higher stability compared to pure NiO. For example, Qi *et al.* have reported the synthesis of a porous and high surface area Ni–Fe oxide through

[a]*Department of Chemistry, Faculty of Science, Universiti Putra Malaysia UPM, 43400 Serdang, Selangor, Malaysia. E-mail: basya@upm.edu.my*

[b]*Integrated Chemical BioPhysics Research, Faculty of Science, Universiti Putra Malaysia UPM, 43400 Serdang, Selangor, Malaysia*

[c]*Department of Chemistry and Earth Sciences, College of Arts and Sciences, Qatar University, Doha 2713, Qatar. E-mail: siham@qu.edu.qa*

† Electronic supplementary information (ESI) available. See DOI: 10.1039/d1ra07304d

a coprecipitation strategy using Tween 85 as an organic surfactant. They revealed that Ni–Fe oxide is highly active for OER, showing low overpotentials of 328 mV and 420 mV at current densities of 10 mA cm^{-2} and 50 mA cm^{-2}, respectively.[29] Similarly, $NiMoO_4$ has been synthesized hydrothermally and evaluated towards OER in an alkaline medium.[27] It shows high electrocatalytic activity in alkaline conditions with an overpotential of 340 mV at a current density of 10 mA cm^{-2}.[27]

The synthesis of hybrid Ni-based electrocatalysts for OER has been accomplished by different methods, such as solvothermal,[30] hydrothermal,[27,31] sol–gel combustion,[32] and coprecipitation.[29] Among them, solution combustion synthesis (SCS) has triggered increased interest assigned to its simplicity, quickness, repeatability, remarkable physiochemical properties, and ability for large-scale synthesis.[33,34] In addition, the resulting products from SCS do not need any purification or post-synthesis treatment. Recently, two nickel-based MTMO have been synthesized through the SCS approach and evaluated as electrocatalysts towards OER. For instance, A. Kumar and coworkers synthesized $NiCoO_2$ through a single-step SCS pathway, using the metal nitrates as oxidant (Ni and Co) and glycine as fuel. They investigated the OER performance of their as-prepared catalyst in 1.0 M KOH solution. They found that the $NiCoO_2$ has a lower Tafel slope value (95 mV dec^{-1}) compared to NiO (114 mV dec^{-1}) and Co_3O_4 (145 mV dec^{-1}), confirming its superior activity and performance towards OER.[35] In the same context, $NiMoO_4$ was synthesized through a low-cost and eco-friendly SCS, using ammonium molybdate tetrahydrate ($(NH_4)_6Mo_7O_{24}\cdot 4H_2O$) and nickel nitrate hexahydrate ($Ni(NO_3)_2\cdot 6H_2O$) as metal precursors, and agar as a fuel. The as-synthesized $NiMoO_4$ has the lower Tafel slope value (48 mV dec^{-1}) compared to NiO (51 mV dec^{-1}), MoO_3 (64 mV dec^{-1}), and commercial $NiMoO_4$ (67 mV dec^{-1}), implying the outstanding OER performance of $NiMnO_4$.[36]

Many researchers synthesized hybrid Ni-based MTMO using SCS and evaluated them as powerful electrocatalysts for OER. To our knowledge, no single study has compared the performance of different MTMO. Triggered by this, herein we reported the synthesis of Ni-based MTMO ($Ni_xM_{1-x}O_y$) using the fast, reliable, and eco-friendly SCS, and we evaluated them towards OER. The as-synthesized electrocatalysts were analyzed by physicochemical spectroscopy and morphology techniques. Their OER activity was assessed using electro-polarization methods (linear sweep voltammetry (LSV), chronoamperometry, chronopotentiometry) and electrochemical impedance spectroscopy.

Materials and method

Chemicals and materials

Nickel(II) nitrate hexahydrate ($Ni(NO_3)_2\cdot 6H_2O$, ACROS Organics, ≥99%), cobalt(II) nitrate hexahydrate ($Co(NO_3)_2\cdot 6H_2O$, BDH, ≥99%), iron(III) nitrate nonahydrate ($Fe(NO_3)_3\cdot 9H_2O$, Sigma Aldrich, ≥98%), manganese nitrate tetrahydrate ($Mn(NO_3)_2\cdot 4H_2O$, Riedel-de Haën, ≥97%), ammonium molybdate tetrahydrate ($(NH_4)_6Mo_7O_{24}\cdot 4H_2O$, BDH, ≥98%), chromium(III) nitrate nonahydrate ($Cr(III)(NO_3)_3\cdot 9H_2O$, Fluka, ≥97%), copper(II) nitrate trihydrate ($Cu(NO_3)_2\cdot 3H_2O$, Carl Roth, ≥98%), glycine (NH_2CH_2COOH, BDH, ≥99%), Nafion perfluorinated resin solution (Sigma Aldrich, 5 wt% in lower aliphatic alcohol and water), and potassium hydroxide (KOH, Carl Roth, 99.98%) were purchased and used without further purification.

Synthesis of NiO by SCS

$Ni(NO_3)_2\cdot 6H_2O$ (872.4 mg, 3 mmol) and glycine (393.8 mg, 5.25 mmol) were weighed together and transferred to a 150 mL beaker containing 50 mL ultrapure water. The mixture was stirred continuously for 30 minutes to assure homogeneity. Afterward, the solution was heated quickly to boil until dryness. Upon dryness combustion occurs quickly with huge fire, getting a friable foam-like nanosized material. The as-synthesized product was transferred to a crucible boat and placed in a furnace oven (550 °C) overnight for calcination purposes.

Synthesis of $Ni_xM_{1-x}O_y$ by SCS

$Ni(NO_3)_2\cdot 6H_2O$ (1454.0 mg, 5 mmol), metal salt source "Co, Fe, Mn, Mo, Cu, or Cr" (1 mmol), and glycine (787.5 mg, 10.5 mmol) were weighed together and transferred to 200 mL beaker containing 50 mL ultrapure water. The mixture was stirred continuously for 30 minutes to assure homogeneity. Afterward, the solution was heated quickly to boil until dryness. Upon dryness combustion occurs quickly with huge fire, getting a friable foam-like nanosized material. The as-synthesized product was transferred to a crucible boat and placed in a furnace oven (550 °C) overnight for calcination purposes.

Material characterization

The size, morphology, and composition of as-synthesized materials were investigated using a field emission scanning electron microscope (FESEM, Philips XL-30, FEI Co., USA) equipped with an energy dispersive X-ray spectrometer (EDX). The powder wide-angle X-ray diffraction patterns (PXRD) were collected from an X'Pert-Pro MPD diffractometer (PANalytical Co., Netherlands) with a CuKα source of radiation ($\lambda = 1.540598$ Å). The elemental oxidation states were investigated by X-ray photoelectron spectroscopy (XPS) using a Kratos Axis Ultra XPS with a monochromatic Al-Kα radiation source (1486.6 eV). The morphology of electrocatalysts was further explored by transmission electron microscopy (TEM) using (FEI, Technai T20, Netherlands) operating at 200 kV. The specific surface area of synthesized materials was studied by from N_2-physisorption experiments at the temperature of liquid nitrogen (77 K) using the BET (Brunauer–Emmett–Teller) method. The pore size and pore volume were estimated from the adsorption branch using the BJH (Barret–Joyner–Halenda) method.

Electrochemical measurements

Electrochemical measurements were performed in a three-electrode system using a glassy carbon electrode (GCE, 5 mm diameter) as a working electrode, Pt wire as an auxiliary electrode, and Ag/AgCl electrode as a reference electrode. The electrolyte for the oxygen evolution reaction was 1.0 M KOH.

The catalyst ink was prepared by dispersing 3 mg of each catalyst in a mixture 900 μL isopropanol and 100 μL Nafion (0.5 wt% in isopropanol). The ink solution was ultrasonicated for 1 hour. After that, 10 μL of the catalyst ink was drop-casted on the glassy carbon electrode and dried in air before electrochemical measurements. The electrochemical measurements were conducted on electrochemical analyzer (reference 3000, Gamry Co., USA).

Prior to measurement, all electrodes were cleaned and activated in N_2-saturated KOH solution for 200 cycles at a scan rate of 100 mV s^{-1}. Polarization curves were recorded as linear sweep voltammetry (LSV) at a scan rate of 50 mV s^{-1}. The electrochemical stability of NiO and $Ni_xM_{1-x}O_y$ were evaluated *via* chronopotentiometric measurements at 10 mA cm^{-2} for 10 h and chronoamperometric experiments at 750 mV *vs.* Ag/AgCl. Electrochemical impedance spectroscopy (EIS) measurements were performed at frequencies varying from 0.1 Hz to 100 kHz with an AC voltage pulse of 10 mV amplitude. The current densities (j) were normalized to the geometric surface area of the working electrode. After measurement, the structural stability of all samples was evaluated by XRD. In the same regard, all catalysts were drop-casted on a fluorine-doped tin oxide (FTO) substrate and analyzed by XRD after electrochemical measurements. The obtained potentials using Ag/AgCl electrode were converted to the reversible hydrogen electrode (RHE) by using the following equation:

$$E(\mathrm{RHE}) = E(\mathrm{Ag/AgCl}) + 0.197 + (0.059 \times \mathrm{pH})$$

All the electrochemical data were 100% *iR*-corrected. The resistances (R) were obtained from the electrochemical impedance spectra.

Results and discussion

Solution combustion synthesis (SCS) is a promising approach for the preparation of nanoscale materials. It includes propagation of self-sustaining exothermic reactions in aqueous solutions. This method is considered as a powerful technique to produce a wide range of nanoscale materials, such as oxides, metals, alloys, and sulfides. SCS can be accomplished in aqueous solution of an oxidizer, usually metal nitrates (often favored because of their oxidizing property and high-water solubility) and a suitable organic fuel (contains C and H atoms) as a reducing agent (*e.g.*, glycine, urea, sucrose, citric acid, *etc.*). Upon heating, the redox mixture is ignited and finally combusts in a self-sustaining rapid combustion reaction, yielding a nanocrystalline materials. Generally, the SCS method produces a substantial amount of gaseous by-products. This gasification causes a substantial expansion of the solid product and a fast drop in temperature after the reaction, resulting in a porous and finely dispersed solid product. These are regarded as the typical features in the SCS of nanoscale materials.[33,34,37] Herein, we synthesized NiO and the hybrid binary $Ni_xM_{1-x}O_y$ materials through solution combustion synthesis pathway by mixing nickel nitrate and metal nitrate precursors such as Co, Fe, Mn, Mo, Cu, or Cr (5 mmol and 1 mmol, respectively) in the presence of glycine as a fuel. The SEM micrographs of NiO and its hybrid materials (Fig. 1) showed porous structure for all materials, which is a common feature of combusted materials. It is attributed to the evolution of a large amount of gases.[34] The EDX analysis confirms the composition of NiO and binary hybrid metal oxides (Fig. S1†). The morphology and particle size of NiO and the binary oxides were further investigated by TEM analysis as displayed in Fig. 2. It shows that spherical shapes were obtained for $Ni_xCo_{1-x}O_y$, $Ni_xMo_{1-x}O_y$, and $Ni_xCr_{1-x}O_y$ (Fig. 2b, e and g, respectively) with an average particle size of 25.9 nm, 24.2 nm, and 29.0 nm, respectively. On the other hand, random agglomerates were obtained for NiO and $Ni_xFe_{1-x}O_y$ and $Ni_xCu_{1-x}O_y$ (Fig. 2a, c and f, respectively), and flakes-like structure for $Ni_xMn_{1-x}O_y$ (Fig. 2d).

It is evident that the surface area and porosity of a catalyst are important parameters which affect the electrocatalytic performance.

This can be attributed to the increase in the surface area that can enlarge the contact area between the electrolyte and the active sites of the catalysts, and hence improving the reaction kinetics.[38–40] In this context, the textural properties of investigated catalysts were studied by N_2-physisorption experiments. The N_2 adsorption–desorption isotherms of NiO and the hybrid binary $Ni_xM_{1-x}O_y$ materials is depicted in Fig. 3. For all investigated catalysts, the isotherm was assigned to be type IV with H3 hysteresis, which is a characteristic feature for mesoporous materials.[41] The surface area, pore volume and pore size for investigated electrocatalysts were calculated using Barret–Joiner–Halenda (BJH) model, and the results are presented in Table 1. The pore size distribution of all synthesized materials is presented in Fig. S2.† It was clearly found that the specific surface area of all investigated catalysts ranges between 6.8 and 29.8 $m^2 g^{-1}$ and pore diameter ranges between 8.5 and 12.3 nm. The pore diameter values confirm that NiO and the other hybrid binary $Ni_xM_{1-x}O_y$ materials are mesoporous materials. The crystalline structure and purity of the synthesized oxides were investigated using XRD measurements. Fig. 4 displays the recorded XRD patterns of NiO and $Ni_xM_{1-x}O_y$'s. The PXRD of NiO is consistent with the cubic NiO (JCPDS 47-1049), it shows well-defined and sharp peaks at $2\theta = 37.2$, 43.4, 62.9, 75.4, and 79.4, which are attributed to the crystal planes (111), (200), (220), (311) and (222), of NiO face-centered cubic (fcc, space group: *Fm3hm*), respectively (Fig. S3†). The XRD pattern of $Ni_xMo_{1-x}O_y$ can be indexed to β-$NiMoO_4$ (JCPDS 12-0348), see Fig. S7.† On the other hand, the XRD patterns of $Ni_xCo_{1-x}O_y$, $Ni_xFe_{1-x}O_y$, $Ni_xMn_{1-x}O_y$, $Ni_xCu_{1-x}O_y$ and $Ni_xCr_{1-x}O_y$ indicate the presence of face-centered cubic structure of NiO with the presence of weak diffraction peaks correspond to trace amount of Co_3O_4 (cubic, *Fd3m*), Fe_3O_4 (cubic, *Fd3m*), Ni_6MnO_8 (fcc, *Fm3m*), CuO (monoclinic, *C2/c*) and Cr_2O_3 (rhombohedral, *R3c*), respectively (Fig. S4–S6 and S8–S9†). Several reports discovered that at lower doping concentration and when the difference between the atomic radii of M^{n+} ($n = 2$, 3 or 4) and Ni^{2+} is not remarkable, Ni^{2+} can be easily replaced with M^{n+} within the same crystal lattice.[42–48] It is known that the atomic radii of Ni^{2+}, Co^{2+}, Fe^{3+}, Mn^{4+}, Cr^{3+} and Cu^{2+} is 0.69 Å, 0.745 Å, 0.645 Å, 0.53

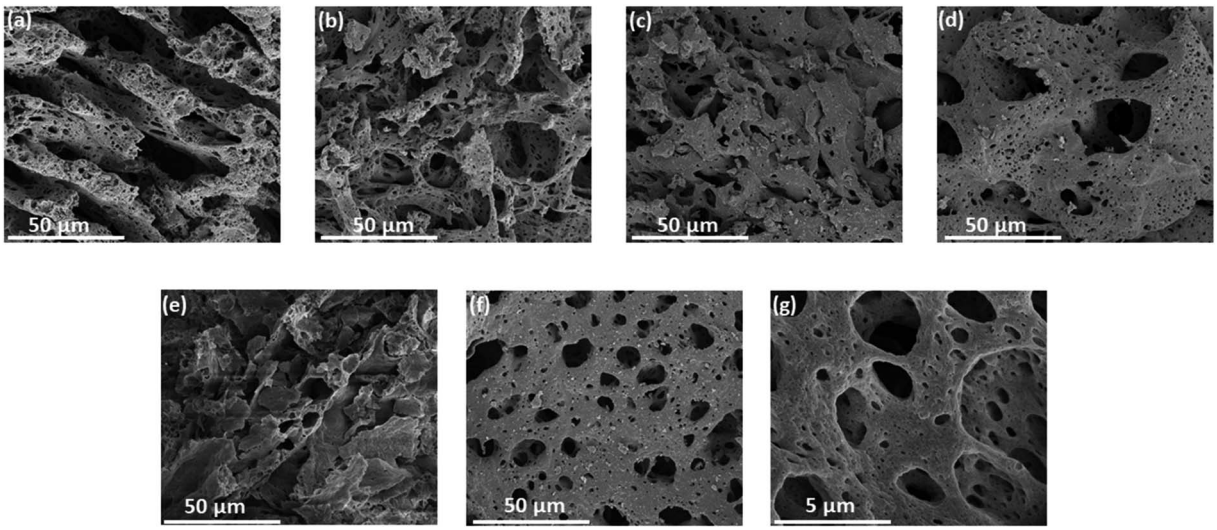

Fig. 1 FESEM images of porous structures of (a) NiO, (b) $Ni_xCo_{1-x}O_y$, (c) $Ni_xFe_{1-x}O_y$, (d) $Ni_xMn_{1-x}O_y$, (e) $Ni_xMo_{1-x}O_y$, (f) $Ni_xCu_{1-x}O_y$ and (g) $Ni_xCr_{1-x}O_y$.

Å, 0.63 Å and 0.73 Å, respectively. This proves that at lower concentration of metal ions doping at NiO, some of the metal ions can replace Ni^{2+} at the rock salt of NiO with the presence of their metal oxide phase in the structure.

The chemical composition and oxidation states of elements in the hybrid binary $Ni_xM_{1-x}O_y$ materials were studied by XPS analysis. The survey spectra revealed the presence of Ni, O, and the corresponding element in each case, confirming their chemical composition (Fig. S10†). The emission spectrum of Ni, O, and other metals was fitted using the Gaussian fitting method. The Ni 2p spectrum is well-fitted with two spin–orbit doublets, which are characteristic of Ni^{2+} and Ni^{3+} (Fig. 5). For Ni^{2+}, the fitting peaks were found in the range 852.7–854.1 eV and 870.3–871.8 eV for $2p_{3/2}$ and $2p_{1/2}$, respectively, whereas

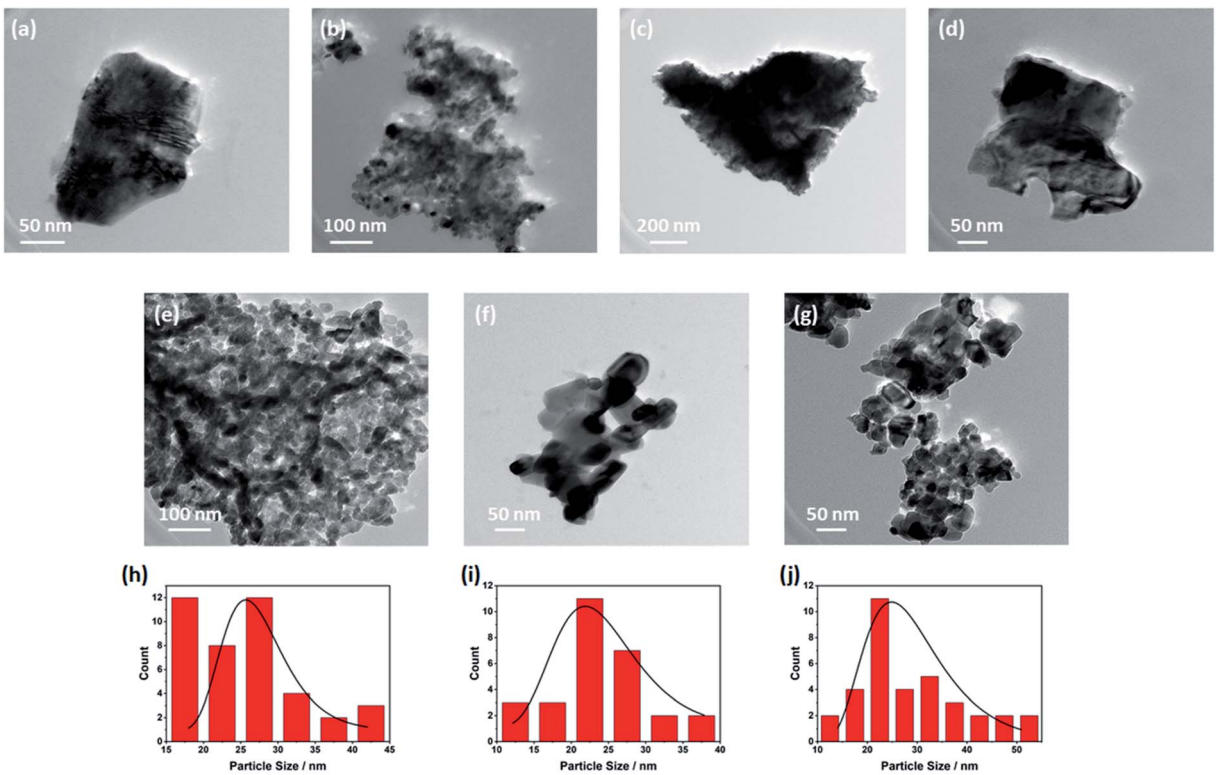

Fig. 2 Morphologies of (a) NiO, (b) $Ni_xCo_{1-x}O_y$, (c) $Ni_xFe_{1-x}O_y$, (d) $Ni_xMn_{1-x}O_y$, (e) $Ni_xMo_{1-x}O_y$, (f) $Ni_xCu_{1-x}O_y$ and (g) $Ni_xCr_{1-x}O_y$. Particle size distribution of (h) $Ni_xCo_{1-x}O_y$, (i) $Ni_xMo_{1-x}O_y$ (j) $Ni_xCr_{1-x}O_y$.

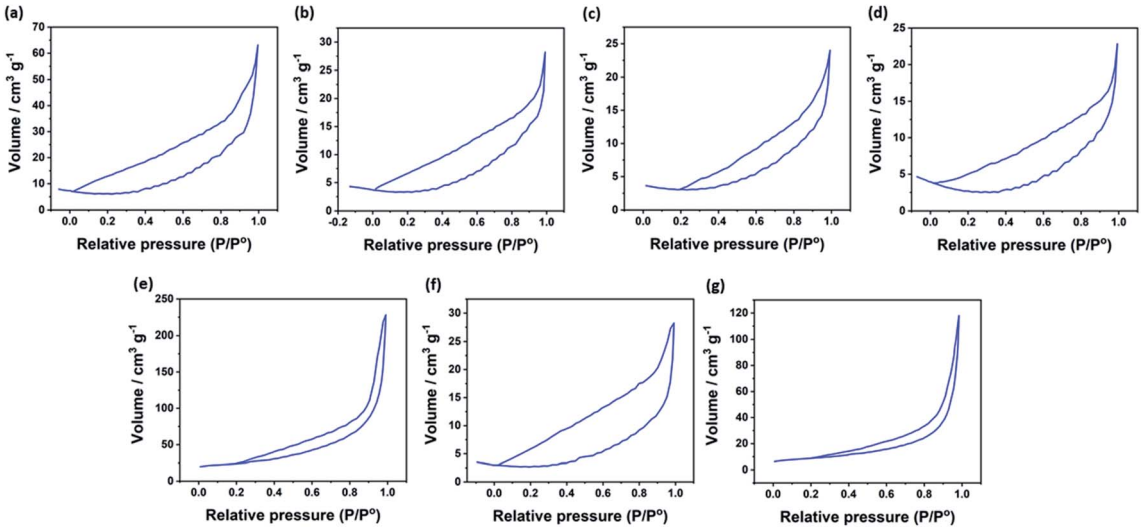

Fig. 3 N_2 adsorption–desorption isotherms of (a) NiO, (b) $Ni_xCo_{1-x}O_y$, (c) $Ni_xFe_{1-x}O_y$, (d) $Ni_xMn_{1-x}O_y$, (e) $Ni_xMo_{1-x}O_y$, (f) $Ni_xCu_{1-x}O_y$ and (g) $Ni_xCr_{1-x}O_y$.

Table 1 Textural properties of NiO and the hybrid binary $Ni_xM_{1-x}O_y$ materials

Catalyst	Surface area ($m^2\ g^{-1}$)	Pore volume ($cm^3\ g^{-1}$)	Pore diameter (nm)
NiO	17.3	0.098298	11.4
$Ni_xCo_{1-x}O_y$	9.8	0.043892	9.0
$Ni_xFe_{1-x}O_y$	8.4	0.037339	8.9
$Ni_xMn_{1-x}O_y$	6.8	0.035503	10.5
$Ni_xMo_{1-x}O_y$	83.4	0.354888	8.5
$Ni_xCu_{1-x}O_y$	7.4	0.043915	11.9
$Ni_xCr_{1-x}O_y$	29.8	0.183563	12.3

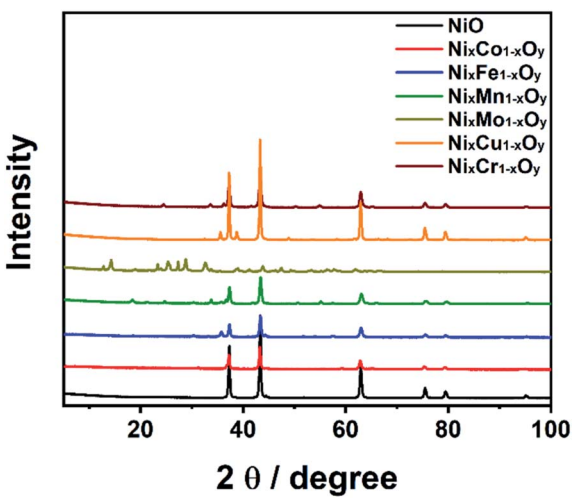

Fig. 4 XRD patterns of $Ni_xM_{1-x}O_y$ materials.

Ni^{3+} were found between 854.7–856.4 eV and 872.9–875.5 eV for $2p_{3/2}$ and $2p_{1/2}$, respectively.[49–55] Two satellite peaks were also observed, which are attributed to bonding between Ni^{2+} and Ni^{3+} with oxygen.[56] The O 1s spectrum is well fitted with three spin–orbit triplets, which are donated with O1, O2 and O3 (Fig. S11†). The peak of O1 is fitted located at 526.7–529.5 eV, and attributed to metal–oxygen bonding, and the peak of O2 lies between 529.4 and 531.4 eV, and correlated to the presence of defect sites related to the low oxygen coordination in small-particle size materials. Finally, the peak of O3 is located between 531.6–533.8 eV, and it can be attributed to the presence of a large number of physically and chemically bonded water molecules on or near the surface.[49] The XPS of Co, Fe, Mn, Mo, Cu, and Cr in the hybrid binary $Ni_xM_{1-x}O_y$ materials revealed two spin–orbit doublets in all spectra. The oxidation states of all elements are as follows: first, the deconvoluted Co 2p spectrum of $Ni_xCo_{1-x}O_y$ showed two peaks for Co^{3+} and Co^{2+} (Fig. 6a).[57] The Fe 2p spectrum for $Ni_xFe_{1-x}O_y$ revealed the presence of Fe^{2+} and Fe^{3+} (Fig. 6b).[58] The deconvoluted Mn 2p spectrum of $Ni_xMn_{1-x}O_y$ revealed the formation of Mn^{4+} and Mn^{3+} oxidation states (Fig. 6c).[51] The fitting of Mo 3d spectrum of $Ni_xMo_{1-x}O_y$ revealed two spin–orbit doublets, characteristic of Mo^{5+} and Mo^{6+} (Fig. 6d).[59] The deconvoluted Cu 2p spectrum for $Ni_xCu_{1-x}O_y$ also shows the formation of a Cu^{+} and Cu^{2+} (Fig. 6e).[53] Finally, the XPS spectrum of $Ni_xCr_{1-x}O_y$ revealed a pair of spin–orbit doublets for Cr^{3+} and Cr^{6+} (Fig. 6f).[55]

The electrocatalytic performance of hybrid binary $Ni_xM_{1-x}O_y$ materials was investigated towards OER in alkaline medium. The majority of mixed metal oxides are suitable catalyst for OER in alkaline medium as their very low stability in acidic medium hindered their performance. In addition, the electrocatalysts for OER are only limited to noble metals and their oxides in acidic media.[60,61] On the other hand, mixed metal oxides have their best performance in alkaline media.[26] This is attributed to their high stability in alkaline medium, excellent oxygen anion mobility, and excellent oxygen exchange kinetics.[26,60,61] The OER mechanism in alkaline medium can be represented by eqn (1)–(5).[62]

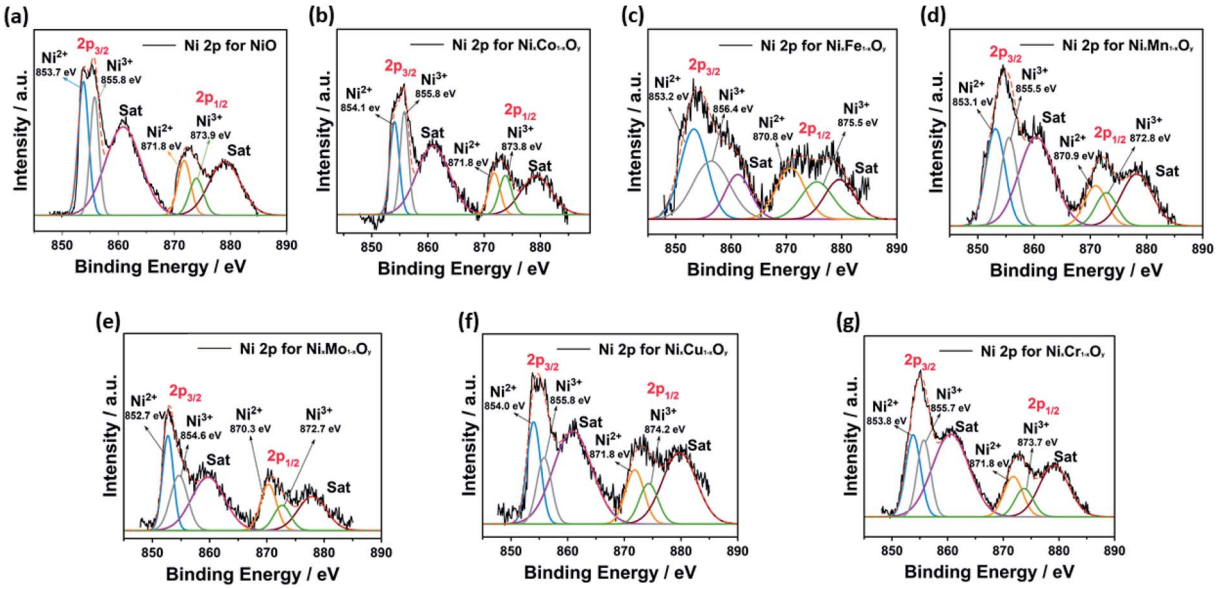

Fig. 5 Ni 2p spectrum for (a) NiO, (b) $Ni_xCo_{1-x}O_y$, (c) $Ni_xFe_{1-x}O_y$, (d) $Ni_xMn_{1-x}O_y$, (e) $Ni_xMo_{1-x}O_y$, (f) $Ni_xCu_{1-x}O_y$ and (g) $Ni_xCr_{1-x}O_y$.

$$M + OH^- \rightarrow MOH \quad (1)$$

$$MOH + OH^- \rightarrow MO + H_2O_{(l)} \quad (2)$$

$$2MO \rightarrow 2M + O_{2(g)} \quad (3)$$

$$MO + OH^- \rightarrow MOOH + e^- \quad (4)$$

$$MOOH + OH^- \rightarrow M + O_{2(g)} + H_2O_{(l)} \quad (5)$$

Ni-based catalysts demonstrated enhanced OER performance in alkaline medium. This was attributed to their advantageous characteristics, such as enhanced reaction kinetics and structure/performance stability.[63] In this context, we studied OER performance of hybrid binary $Ni_xM_{1-x}O_y$ materials in 1.0 M KOH solution. Fig. 7a represents LSV of $Ni_xM_{1-x}O_y$ materials. The onset potential of the electrocatalysts follows the following order $Ni_xCo_{1-x}O_y$ < $Ni_xMo_{1-x}O_y$ < $Ni_xFe_{1-x}O_y$ < $Ni_xCr_{1-x}O_y$ < $Ni_xCu_{1-x}O_y$ < $Ni_xMn_{1-x}O_y$ < NiO. This

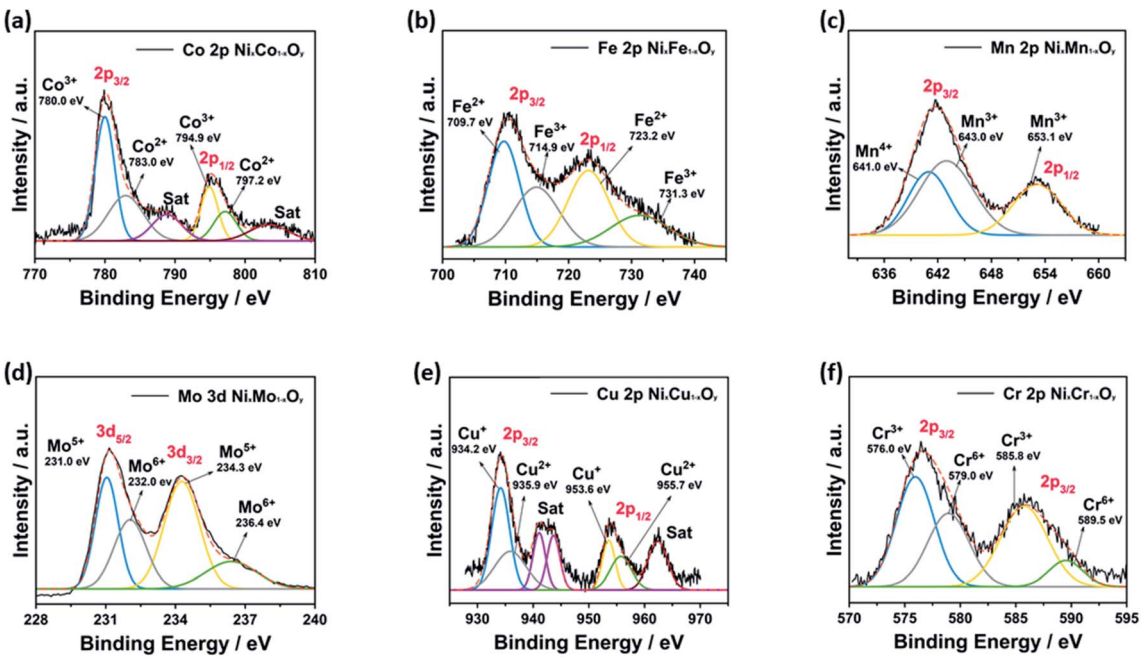

Fig. 6 XPS analysis of (a) Co 2p of $Ni_xCo_{1-x}O_y$ (b) Fe 2p of $Ni_xFe_{1-x}O_y$, (c) Mn 2p of $Ni_xMn_{1-x}O_y$, (d) Mo 3d of $Ni_xMo_{1-x}O_y$, (e) Cu 2p of $Ni_xCu_{1-x}O_y$, (f) Cr 2p of $Ni_xCr_{1-x}O_y$.

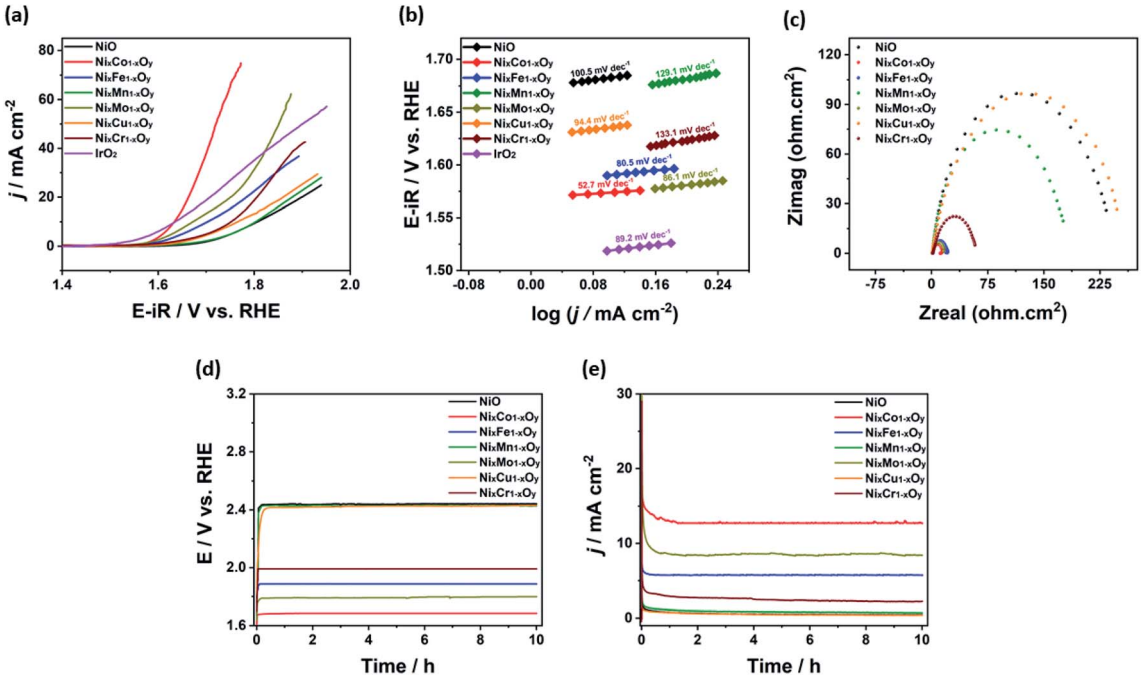

Fig. 7 (a) LSV curves of NiO and $Ni_xM_{1-x}O_y$ (including IrO_2), (b) Tafel plots, (c) Nyquist plots (d) chronopotentiometric response of NiO and $Ni_xM_{1-x}O_y$ at the applied current density of 10 mA cm^{-2} *vs.* RHE in 1.0 M KOH electrolyte (e) chronoamperometric response of NiO and $Ni_xM_{1-x}O_y$ at the applied potential of 750 mV *vs.* RHE in 1.0 M KOH electrolyte.

confirms that the positive impact of doping Ni with other metals. OER activity was further evaluated by the value of overpotentials measured at a current density of 10 mA cm^{-2} (η_{10}) and 1 mA cm^{-2} (η_1). The calculated values for η_{10} were 585, 404, 473, 573, 442, 535, and 522 mV and for η_1 were 443, 339, 353, 426, 344, 397, and 367 mV for NiO, $Ni_xCo_{1-x}O_y$, $Ni_xFe_{1-x}O_y$, $Ni_xMn_{1-x}O_y$, $Ni_xMo_{1-x}O_y$, $Ni_xCu_{1-x}O_y$, and $Ni_xCr_{1-x}O_y$, respectively. This demonstrates the preferential OER of the hybrid binary $Ni_xM_{1-x}O_y$ materials compared to NiO.

In addition, to obtain more insights about the OER kinetics of our electrocatalysts, the Tafel slopes were evaluated by measuring the slope of the linear part of the polarization curve (Fig. 7b). The values of Tafel slope were 100.5, 52.7, 80.5, 129.1, 86.1, 94.4, 133.1, and 89.2 mV dec^{-1} for NiO, $Ni_xCo_{1-x}O_y$, $Ni_xFe_{1-x}O_y$, $Ni_xMn_{1-x}O_y$, $Ni_xMo_{1-x}O_y$, $Ni_xCu_{1-x}O_y$, $Ni_xCr_{1-x}O_y$, and IrO_2, respectively. This implies the enhanced OER performance of $Ni_xCo_{1-x}O_y$ electrocatalyst compared to the other hybrid binary Ni-based electrocatalysts. Table 2 summarizes the OER performance of some common electrocatalysts compared with $Ni_xCo_{1-x}O_y$.

The kinetics of the investigated electrocatalysts were studied using electrochemical impedance spectroscopy (EIS). Fig. 7c depicted the Nyquist plots of NiO and $Ni_xMo_{1-x}O_y$ in 1.0 M KOH solution. The plots show enhanced OER kinetics acquired by coupling Ni with other transition metals compared to NiO, Fig. 7c. It was clear that the radius of semicircle Nyquist plots decreased with increasing the performance of OER. Among the hybrid binary $Ni_xM_{1-x}O_y$ materials, $Ni_xCo_{1-x}O_y$ expressed the lowest charge transfer resistance, it has the smallest radius in semicircular Nyquist plots, suggesting faster charge transfer of charged species such as electron and OH^- (electrons and OH^- ions). This can be attributed to high oxidation state of Co^{3+} and Ni^{3+} existed in $Ni_xCo_{1-x}O_y$, which can be confirmed from the deconvoluted fitted peaks under Ni 2p and Co 2p XPS spectra. It was clearly observed that the area ratio of Ni^{3+}/Ni^{2+} for $Ni_xCo_{1-x}O_y$ was found to be 1.01 which is higher than other materials 0.75, 0.88, 0.77, 0.92, 0.77, and 0.85 for NiO, $Ni_xFe_{1-x}O_y$, $Ni_xMn_{1-x}O_y$, $Ni_xMo_{1-x}O_y$, $Ni_xCu_{1-x}O_y$, and $Ni_xCr_{1-x}O_y$, respectively. In addition, the area ratio of Co^{3+}/Co^{2+} was the highest for $Ni_xCo_{1-x}O_y$ (1.51) compared to the area ratio of Fe^{3+}/Fe^{2+} in $Ni_xFe_{1-x}O_y$ (0.81), Mn^{4+}/Mn^{3+} in $Ni_xMn_{1-x}O_y$ (0.65), Mo^{6+}/Mo^{5+} (0.87), Cu^{2+}/Cu^{+} (0.67) and Cr^{6+}/Cr^{3+} (0.71). Several reports stated that the higher oxidation state speeds us and eases the charge transfer during the catalytic reaction in alkaline electrolytes leading to better performance on OER activity.[11,64,65]

The electrochemical stability of the hybrid binary $Ni_xM_{1-x}O_y$ materials was studied by chronoamperometric (*j*–*t*) and chronopotentiometric (*E*–*t*) measurements (Fig. 7d and e). The chronoamperometric measurement was performed at a fixed overpotential of 0.750 V in 1.0 M KOH solution *versus* Ag/AgCl electrode. It was clearly observed that there was no observed potential decay in curves for all prepared electrocatalysts until 10 hours. $Ni_xCo_{1-x}O_y$ had the highest current density at 0.750 V compared to other electrocatalysts, confirming its superior activity towards OER. In addition, the chronopotentiometric measurement was performed at a fixed current density of 10 mA cm^{-2} in 1.0 M KOH solution *versus* Ag/AgCl. It was noticeable that there was no current decay in all electrocatalysts. Similar to *E*–*t* measurements, $Ni_xCo_{1-x}O_y$ displayed stability at the highest

Table 2 OER performance of $Ni_xCo_{1-x}O_y$ in 1.0 M KOH solution compared with literature

Catalyst	Electrolyte	η_1 @1 mA cm^{-2} (mV)	η_{10} @10 mA cm^{-2} (mV)	Tafel slope (mV dec^{-1})	Ref.
$Ni_xCo_{1-x}O_y$	1.0 M KOH	339	404	52.7	This work
CuO-from Cu-EA	1.0 M KOH	370	475	90	2
Co_3O_4	0.1 M KOH	—	450	89	5
F-Ni-2	1.0 M KOH	—	330	53	7
F-NiAl LDH-NF	1.0 M KOH	—	250	77	7
PtNi/Mn_2O_3–NiO	0.1 M KOH	—	529	140	8
RuO_2/Co_3O_4	1.0 M KOH	—	305	69	14
Ir/Ni oxide	1.0 M KOH		264	31	15
$NiCo_2O_4$ nanoflowers	1.0 M KOH	—	383	137	18
$NiCo_2O_4$ hollow nanospheres	1.0 M KOH	—	428	141	18
MoO_3/Ni–NiO	1.0 M KOH	347 @100 mA cm^{-2}	—	60	19
10% Ni-doped Mn_3O_4	1.0 M KOH	235 @5 mA cm^{-2}	283	165	20
NG02 ($NiFe_2O_4$/rGO 2 : 5 wt%)	1.0 M KOH	—	302	63	21
NiO/NF	1.0 M KOH	—	310	54	22
$NiCo_2O_4$	1.0 M KOH	—	292	62	23
$NiCo_2O_4$/rGO (nanonet)	0.1 M KOH	—	450	53	25
$NiCo_2O_4$/rGO (microsphere)	0.1 M KOH	—	510	62	25
$NiMoO_4$ nanorods	1.0 M KOH	—	340	45.6	27
Cu_2O–Cu hybrid foams	1.0 M KOH	—	250	67.52	28
Ni–Fe oxide	0.1 M KOH	420 @50 mA cm^{-2}	328	42	29
$Co_{0.25}Ni_{0.75}Fe_2O_4$	1.0 M KOH	380 @5 mA cm^{-2}	450	50.5	32
$Co_{0.5}Ni_{0.5}Fe_2O_4$	1.0 M KOH	418 @5 mA cm^{-2}	477	73.0	32
$Co_{0.75}Ni_{0.25}Fe_2O_4$	1.0 M KOH	401 @5 mA cm^{-2}	460	52.2	32

overpotential when compared to other catalysts. This result is consistent with *E–t* measurements, LSV, and Tafel plots. To confirm the structural stability of the investigated electrocatalysts, XRD of samples after activity was performed, Fig. S12–S18.† It was found that the investigated electrocatalyst was stable and maintained crystallinity after measurement, which confirms the high stability of our electrocatalysts.

Several reports demonstrated that the presence of a high-valence state ion like Ni^{3+} is considered as real active sites of OER.[66,67] In addition, coupling Ni to the higher oxidation states of other metal oxides *i.e.*, Co^{3+}, Fe^{3+}, Mo^{6+}, and Cr^{3+} enhanced the OER performance of hybrid materials.[27,35,36,55,58] For example, $NiCoO_2$ has an improved performance towards OER more than Co_3O_4 and NiO.[35] This is due to the presence of a higher ratio of higher oxidation states species (Ni^{3+} and Co^{3+}) on the surface compared to lower oxidation states species (Ni^{2+} and Co^{2+}).[35] This facilitates the charge carrier transfer across the catalyst/electrolyte interface, hence enhancing OER activity.[35] Similarly, the presence of Fe^{3+} ion in the crystal lattice increases the conductivity of the catalytic sites. This suppresses the metal oxidation step and facilitates the metal reduction evolving step of O_2 which results in enhancing the OER performance.[68] This was proved by Xie *et al.* when they introduced a small amount of Fe_3O_4 species into a Ni/NiO. The charge transfer between Ni and Fe sites improved and provided more active sites for OER.[58] In addition, it was reported that the presence of Mo^{6+} oxidation state as a dopant in NiFe alloy or as a part of crystal lattice in $CaMoO_4$ boosted the OER activity.[69] The presence of Mo in $NiMoO_4$ enhanced the charge transfer process and promoted the generation of Ni^{3+} species, resulting in enhanced performance of OER compared to the bare MoO_3 and NiO.[27,36] According to earlier reports, the multivalent characteristics of Cr can also enable significant electron interactions inside the matrix of transition-metal complexes, therefore improving metal–metal synergy toward OER and hence catalytic activity.[55] The electron configuration of Cr^{3+} is most likely $t_{2g}^3e_g^0$, and this electron configuration is favorable for charge transfer and electron capture. As a result, Cr^{3+} can significantly enhance the formation Ni^{3+} species thus boost the OER activity.[55] On the other hand, some reports stated that the presence of Mn and Cu with NiO might suppress the catalytic OER performance of their metals. Mn has been known to suppress the OER activity attributed to Jahn–Teller distortion, which causes suppression of OER activity. This is due to the octahedral position which is occupied by the Jahn–Teller active Mn^{3+}, which decreases the OER activity.[70] Also, thermodynamic studies revealed that Cu species do not undergo redox process in the same potential region that nickel species do. This leads to minimizing the formation of Ni^{3+} species during the OER process, thus suppressing the OER performance.[48]

According to the discussions above and to our electrocatalytic investigations, the superior OER performance of Ni_x-$Co_{1-x}O_y$ can be assigned based on the following factors; first, the presence of Co^{3+} facilitates and accelerates the oxidation of Ni^{2+} to Ni^{3+} more than other metal ions. This can be clearly evidenced by deconvoluted XPS spectra of hybrid binary Ni_x-$M_{1-x}O_y$ materials (Fig. 5, 6 and Table 1S†), where the area of deconvoluted $2p_{3/2}$ peak ratio of Ni^{3+}/Ni^{2+} was obtained the highest amongst other investigated electrocatalysts. Second, from the deconvoluted XPS spectra, the ratio of the area of deconvoluted $2p_{3/2}$ peak Co^{3+}/Co^{2+} was the highest when compared to other metals (see Table 1S†). As previously

reported, the increase of higher oxidation states in metal oxides enhances the OER activity.[11,64,65] Based on this, the activity of hybrid binary $Ni_xM_{1-x}O_y$ materials followed the same trend seen in the area ratio of Ni^{3+}/Ni^{2+} and area ratio of M^n/M^{n+m} ($Ni_xCo_{1-x}O_y$ < $Ni_xMo_{1-x}O_y$ < $Ni_xFe_{1-x}O_y$ < $Ni_xCr_{1-x}O_y$ < $Ni_xCu_{1-x}O_y$ < $Ni_xMn_{1-x}O_y$ < NiO). On the other hand, $Ni_xMn_{1-x}O_y$ showed the lowest activity amongst all electrocatalysts. Our result was consistent with those reported for Mn-doped metal oxide, where they exhibited the lowest activities towards OER amongst other mixed metal oxides.[71,72]

Conclusions

In summary, this work has demonstrated the higher OER performance of the hybrid binary $Ni_xM_{1-x}O_y$ materials compared to bare NiO. These mesoporous nanomaterials with enhanced OER activity were synthesized by fast and economic solution combustion synthesis. They depicted porous nature with surface area ranging between 7.4 and 83.4 $m^2\ g^{-1}$. In addition, the hybrid catalysts revealed a well crystalline structure. XPS spectra showed a mixed oxidation states for all transition metals with $Ni_xCo_{1-x}O_y$ revealing the highest content of high oxidation state. The hybrid binary $Ni_xM_{1-x}O_y$ materials showed higher OER performance than their consistent NiO in alkaline medium. $Ni_xCo_{1-x}O_y$ exhibited the highest performance amongst other investigated electrocatalysts. It displays an overpotential of 339 mV and 404 mV at a current density of @1 mA cm^{-2} and @10 mA cm^{-2}, respectively, and a Tafel slope of 52.7 mV dec^{-1} in 1.0 M KOH solution. While the overpotential of other electrocatalysts ranges between 344–443 mV and 442–585 mV @1 mA cm^{-2} and @10 mA cm^{-2}, respectively, and the Tafel slope ranges between 80.5-133.1 mV dec^{-1}. The superior activity of hybrid binary $Ni_xCo_{1-x}O_y$ is attributed to synergistic effect between Ni and cobalt, and the amount of Ni^{3+} and Co^{3+} on surface. The research outcomes reveal a promising application of combusted nanomaterials toward OER in the future.

Conflicts of interest

There are no conflicts to declare.

Acknowledgements

The authors acknowledge the technical support of Central Laboratories Unit (CLU), Center for Advanced Materials (CAM), and Gas Processing Center (GPC), Qatar University, Doha, Qatar.

References

1 Y. Lin, Z. Tian, L. Zhang, J. Ma, Z. Jiang, B. J. Deibert, R. Ge and L. Chen, *Nat. Commun.*, 2019, **10**, 162.
2 X. Liu, S. Cui, M. Qian, Z. Sun and P. Du, *Chem. Commun.*, 2016, **52**, 5546–5549.
3 S. Yan, Y. Xue, S. Li, G. Shao and Z. Liu, *Int. J. Hydrogen Energy*, 2020, **45**, 1846–1856.
4 M. Favaro, W. S. Drisdell, M. A. Marcus, J. M. Gregoire, E. J. Crumlin, J. A. Haber and J. Yano, *ACS Catal.*, 2017, **7**, 1248–1258.
5 L. Li, T. Tian, J. Jiang and L. Ai, *J. Power Sources*, 2015, **294**, 103–111.
6 S. W. Lee, C. Baik, T.-Y. Kim and C. Pak, *Catal. Today*, 2020, **352**, 39–46.
7 Y. Tong, H. Mao, P. Chen, Q. Sun, F. Yan and F. Xi, *Chem. Commun.*, 2020, **56**, 4196–4199.
8 D. Mladenović, D. M. F. Santos, G. Bozkurt, G. S. P. Soylu, A. B. Yurtcan, Š. Miljanić and B. Šljukić, *Electrochem. Commun.*, 2021, **124**, 106963.
9 C. Huang, Q. Ji, H. Zhang, Y. Wang, S. Wang, X. Liu, Y. Guo and C. Zhang, *J. Colloid Interface Sci.*, 2022, **606**, 654–665.
10 X. F. Lu, Y. Chen, S. Wang, S. Gao and X. W. Lou, *Adv. Mater.*, 2019, **31**, 1902339.
11 J. Bian, Z. Li, N. Li and C. Sun, *Inorg. Chem.*, 2019, **58**, 8208–8214.
12 Y. Wu, M. Tariq, W. Q. Zaman, W. Sun, Z. Zhou and J. Yang, *ACS Appl. Energy Mater.*, 2019, **2**, 4105–4110.
13 S. D. Ghadge, P. P. Patel, M. K. Datta, O. I. Velikokhatnyi, R. Kuruba, P. M. Shanthi and P. N. Kumta, *RSC Adv.*, 2017, **7**, 17311–17324.
14 H. Liu, G. Xia, R. Zhang, P. Jiang, J. Chen and Q. Chen, *RSC Adv.*, 2017, **7**, 3686–3694.
15 L. Gong, D. Ren, Y. Deng and B. S. Yeo, *ACS Appl. Mater. Interfaces*, 2016, **8**, 15985–15990.
16 T. Gao, Z. Jin, M. Liao, J. Xiao, H. Yuan and D. Xiao, *J. Mater. Chem. A*, 2015, **3**, 17763–17770.
17 T. Maiyalagan, K. A. Jarvis, S. Therese, P. J. Ferreira and A. Manthiram, *Nat. Commun.*, 2014, **5**, 3949.
18 Z. Li, B. Li, J. Chen, Q. Pang and P. Shen, *Int. J. Hydrogen Energy*, 2019, **44**, 16120–16131.
19 X. Li, Y. Wang, J. Wang, Y. Da, J. Zhang, L. Li, C. Zhong, Y. Deng, X. Han and W. Hu, *Adv. Mater.*, 2020, **32**, 2003414.
20 V. Maruthapandian, T. Pandiarajan, V. Saraswathy and S. Muralidharan, *RSC Adv.*, 2016, **6**, 48995–49002.
21 P. Shinde, C. S. Rout, D. Late, P. K. Tyagi and M. K. Singh, *Int. J. Hydrogen Energy*, 2021, **46**, 2617–2629.
22 P. T. Babar, A. C. Lokhande, M. G. Gang, B. S. Pawar, S. M. Pawar and J. H. Kim, *J. Ind. Eng. Chem.*, 2018, **60**, 493–497.
23 C. L. I. Flores and M. D. L. Balela, *J. Solid State Electrochem.*, 2020, **24**, 891–904.
24 M. L. Lindstrom, R. Gakhar, K. Raja and D. Chidambaram, *J. Electrochem. Soc.*, 2020, **167**, 046507.
25 E. Umeshbabu, G. Rajeshkhanna, P. Justin and G. R. Rao, *J. Solid State Electrochem.*, 2016, **20**, 2725–2736.
26 Y. H. Ahmad, K. A. Eid, S. Y. AlQaradawi and N. K. Allam, *Sustainable Energy Fuels*, 2017, **1**, 1123–1129.
27 X. Zhao, J. Meng, Z. Yan, F. Cheng and J. Chen, *Chin. Chem. Lett.*, 2019, **30**, 319–323.
28 H. Xu, J.-X. Feng, Y.-X. Tong and G.-R. Li, *ACS Catal.*, 2017, **7**, 986–991.
29 J. Qi, W. Zhang, R. Xiang, K. Liu, H.-Y. Wang, M. Chen, Y. Han and R. Cao, *Adv. Sci.*, 2015, **2**, 1500199.

30 J. Zhang, B. Yuan, S. Cui, N. Zhang, J. Wei, X. Wang, D. Zhang, R. Zhang and Q. Huo, *Dalton Trans.*, 2017, **46**, 3295–3302.
31 J. Wang, Y. Fu, Y. Xu, J. Wu, J.-H. Tian and R. Yang, *Int. J. Hydrogen Energy*, 2016, **41**, 8847–8854.
32 V. Maruthapandian, M. Mathankumar, V. Saraswathy, B. Subramanian and S. Muralidharan, *ACS Appl. Mater. Interfaces*, 2017, **9**, 13132–13141.
33 F.-t. Li, J. Ran, M. Jaroniec and S. Z. Qiao, *Nanoscale*, 2015, **7**, 17590–17610.
34 A. Varma, A. S. Mukasyan, A. S. Rogachev and K. V. Manukyan, *Chem. Rev.*, 2016, **116**, 14493–14586.
35 A. Ashok, A. Kumar, J. Ponraj, S. A. Mansour and F. Tarlochan, *Int. J. Hydrogen Energy*, 2019, **44**, 16603–16614.
36 M. B. Rammal and S. Omanovic, *Mater. Chem. Phys.*, 2020, **255**, 123570.
37 S. L. González-Cortés and F. E. Imbert, *Appl. Catal., A*, 2013, **452**, 117–131.
38 S. Al Khateeb and T. D. Sparks, *J. Mater. Res.*, 2019, **34**, 2456–2471.
39 S. A. Khateeb, A. G. Lind, R. Santos-Ortiz, N. D. Shepherd and K. S. Jones, *J. Electrochem. Soc.*, 2015, **162**, A1667–A1674.
40 S. Al Khateeb, A. G. Lind, R. Santos-Ortiz, N. D. Shepherd and K. S. Jones, *J. Mater. Sci.*, 2015, **50**, 5174–5182.
41 F. Adam and I. A. Sugiarmawan, *J. Porous Mater.*, 2008, **16**, 321.
42 S. Hasan, R. A. Mayanovic and M. Benamara, *AIP Adv.*, 2018, **8**, 056305.
43 R. Sharma, A. D. Acharya, S. Moghe, S. B. Shrivastava, M. Gangrade, T. Shripathi and V. Ganesan, *Mater. Sci. Semicond. Process.*, 2014, **23**, 42–49.
44 Y. Dong, J. Yang, Y. Liu, Y. Wang, Z. Dong, M. Cui, M. Li, X. Yuan, X. Zhang and X. Dai, *Dalton Trans.*, 2020, **49**, 6355–6362.
45 J. Wang, J. Cai, Y.-H. Lin and C.-W. Nan, *Appl. Phys. Lett.*, 2005, **87**, 202501.
46 S. Hasan, R. A. Mayanovic and M. Benamara, *MRS Adv.*, 2017, **2**, 3465–3470.
47 M. Shkir, V. Ganesh, S. AlFaify, I. S. Yahia and H. Y. Zahran, *J. Mater. Sci.: Mater. Electron.*, 2018, **29**, 6446–6457.
48 A. C. Tavares, M. A. M. Cartaxo, M. I. da Silva Pereira and F. M. Costa, *J. Electroanal. Chem.*, 1999, **464**, 187–197.
49 J. Zhang, F. Liu, J. P. Cheng and X. B. Zhang, *ACS Appl. Mater. Interfaces*, 2015, **7**, 17630–17640.
50 J. Jiang, C. Zhang and L. Ai, *Electrochim. Acta*, 2016, **208**, 17–24.
51 X. Liu, J. Cao, C. Huang, Z. Chen, X. Fan, K. Shi, Z. Yang and W. Zhang, *Mater. Res. Express*, 2020, **7**, 065502.
52 K. O. Egbo, S. K. Shil, C. G. Kwok, Y. Wang, C. P. Liu and K. M. Yu, *J. Alloys Compd.*, 2021, **876**, 160136.
53 Z. Fang, S. u. Rehman, M. Sun, Y. Yuan, S. Jin and H. Bi, *J. Mater. Chem. A*, 2018, **6**, 21131–21142.
54 Y. Wu, F. Li, W. Chen, Q. Xiang, Y. Ma, H. Zhu, P. Tao, C. Song, W. Shang, T. Deng and J. Wu, *Adv. Mater.*, 2018, **30**, 1803151.
55 X. Liu and J. Wu, *Electrochim. Acta*, 2019, **320**, 134577.
56 J. Liao, Y. Feng, W. Lin, X. Su, S. Ji, L. Li, W. Zhang, B. G. Pollet and H. Li, *Int. J. Hydrogen Energy*, 2020, **45**, 8168–8176.
57 S. Chandra Sekhar, G. Nagaraju and J. S. Yu, *Nano Energy*, 2018, **48**, 81–92.
58 Y. Xie, X. Wang, K. Tang, Q. Li and C. Yan, *Electrochim. Acta*, 2018, **264**, 225–232.
59 W. Fang, P. Wang, Z. Ni, T. Sun, C. Xiang, K. Yue, R. Wang, J. Yang, Y. Zhou, C. Wang and Y. Yang, *Adv. Mater. Interfaces*, 2020, **7**, 2000754.
60 D. Chen, C. Chen, Z. M. Baiyee, Z. Shao and F. Ciucci, *Chem. Rev.*, 2015, **115**, 9869–9921.
61 C. Hu, L. Zhang and J. Gong, *Energy Environ. Sci.*, 2019, **12**, 2620–2645.
62 N. Yuan, Q. Jiang, J. Li and J. Tang, *Arabian J. Chem.*, 2020, **13**, 4294–4309.
63 Y. Chen, K. Rui, J. Zhu, S. X. Dou and W. Sun, *Chem.–Eur. J.*, 2019, **25**, 703–713.
64 C. X. Guo and C. M. Li, *Chem. Commun.*, 2018, **54**, 3262–3265.
65 Y. Yan, C. Liu, H. Jian, X. Cheng, T. Hu, D. Wang, L. Shang, G. Chen, P. Schaaf, X. Wang, E. Kan and T. Zhang, *Adv. Funct. Mater.*, 2021, **31**, 2009610.
66 S. Ni, H. Qu, H. Xing, Z. Xu, X. Zhu, M. Yuan, L. Wang, J. Yu, Y. Li, L. Yang and H. Liu, *ACS Appl. Mater. Interfaces*, 2021, **13**, 17501–17510.
67 Y. Wang, S. Tao, H. Lin, S. Han, W. Zhong, Y. Xie, J. Hu and S. Yang, *RSC Adv.*, 2020, **10**, 33475–33482.
68 S. Anantharaj, S. Kundu and S. Noda, *Nano Energy*, 2021, **80**, 105514.
69 M.-I. Jamesh and X. Sun, *J. Power Sources*, 2018, **400**, 31–68.
70 S. Hirai, S. Yagi, A. Seno, M. Fujioka, T. Ohno and T. Matsuda, *RSC Adv.*, 2016, **6**, 2019–2023.
71 B. Han, M. Risch, Y.-L. Lee, C. Ling, H. Jia and Y. Shao-Horn, *Phys. Chem. Chem. Phys.*, 2015, **17**, 22576–22580.
72 M. Li, Y. Xiong, X. Liu, X. Bo, Y. Zhang, C. Han and L. Guo, *Nanoscale*, 2015, **7**, 8920–8930.